ORIGINAL ARTICLE

lajss.org Latin American Journal of Solids and Structures

www.lajss.org

A computational model for the mass and geometric dispersion of target-derived debris generated by rod penetration of finite-thickness steel plates

Xiaotong Qi[a], Yangziyi Ji[b], Xiangdong Li[a]*, Lanwei Zhou[a]*

[a] Nanjing University of Science and Technology; Nanjing, 210094, China. Email: qixiaotong@njust.edu.cn, lixiangd@njust.edu.cn, lwzhou@njust.edu.cn:

[b] School of Mechanical Engineering, Nanjing Institute of Technology, Nanjing, China. Email: jyzy525@hotmail.com:

* Corresponding author

https://doi.org/10.1590/1679-7825/e9223

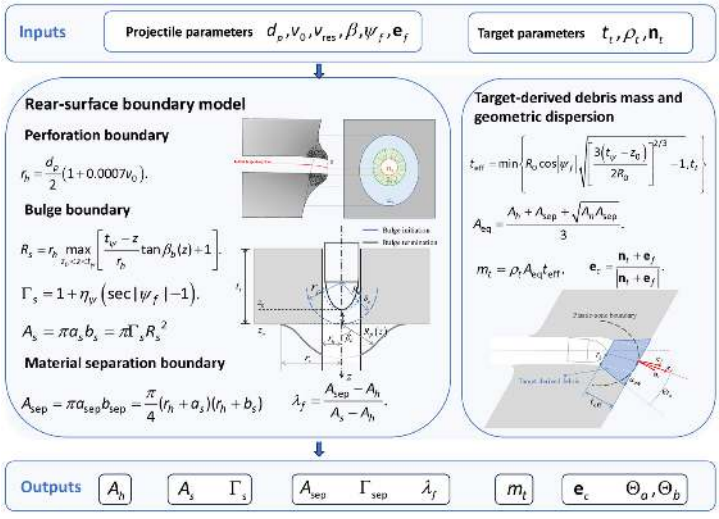
Abstract

A computational model is developed to estimate the mass and geometric dispersion of target-plate-sourced debris from rod penetration of finite-thickness steel plates. Perforation, material-separation, and bulge regions represent the rear surface. Their boundaries are calculated from penetration-state parameters, cavity-expansion theory, and the Ravid–Bodner spherical-cap formulation, with a correction for oblique penetration. Debris mass is obtained from an equivalent source volume and effective participating thickness. The rear-surface normal, exit direction, and source-region expansion define the central direction and equivalent dispersion half-angles. Validation uses boundary data from eight shots, recovered masses from three shots, and first-witness perforations from three shots. Mean relative errors for the boundary areas are 11.42%, 17.22%, and 9.13%, and the mass error is 9.41%. Predicted ranges contain over 97% of the perforation centers. The model captures radial extent under normal penetration and transverse extent under oblique penetration, but overpredicts incidence-plane extent.

Keywords

Rod penetrator; Finite-thickness steel plate; Target-derived debris; Material separation boundary; Debris mass; Geometrically equivalent dispersion half-angle.

Graphical abstract



Received August 01, 2026. In revised form August 10, 2026. Accepted August 10, 2026. Available online August 19, 2026.
https://doi.org/10.1590/1679-7825/e9223

Latin American Journal of Solids and Structures. ISSN 1679-7825. Copyright © **2026**. This is an Open Access article distributed under the terms of the Creative Commons Attribution License, which permits unrestricted use, distribution, and reproduction in any medium, provided the original work is properly cited.

1. INTRODUCTION

When a long-rod penetrator perforates a finite-thickness steel plate, the residual penetrator enters the space behind the target together with behind-armor debris (BAD). BAD comprises penetrator-derived debris produced by penetrator erosion or fracture and target-plate-sourced debris separated during perforation and rear-surface failure. Its mass and spatial distribution govern the debris loading on personnel, equipment, and critical components within armored structures and are important for vulnerability and damage assessment.

Methods for predicting the ballistic limit, residual velocity, exit attitude, and failure of finite-thickness steel targets are well established. Recht and Ipson (1963) related ballistic limit to residual velocity, while Backman and Goldsmith (1978) reviewed penetration processes and failure modes over a range of target thicknesses and impact velocities. Later studies examined the effects of target material strength, shear plugging, and penetrator nose shape on perforation (Børvik et al., 1999; Dey et al., 2004). Đurović et al. (2025) incorporated shear-plugging-induced changes in effective target thickness into a perforation model, and Ma et al. (2025) investigated penetrator exit attitude and spaced-target failure under oblique penetration. Forrestal and Luk (1988) used cavity-expansion theory to estimate the plastic region around the penetration channel. Ravid and Bodner (1983) described plate perforation and rear-surface bulging in stages and represented the bulge boundary using spherical-cap geometry. Chocron et al. (2003) coupled this formulation with a long-rod penetration model to calculate penetration, bulging, and exit failure.

BAD studies have addressed debris formation, spatial distribution, experimental characterization, and vulnerability assessment. Yarin et al. (2000) modeled fragmentation of penetrator and target materials and BAD formation, while Yossifon and Yarin (2002) analyzed debris formation using failure-state variables obtained from finite-element simulations. Mayseless et al. (1992) described debris-field expansion using distribution functions and ellipsoidal geometry. Hartmann (2005) reviewed physical, empirical, and statistical BAD models, while Arnold and Paul (2001) applied debris-field descriptions to armored-vehicle vulnerability assessment. Recent studies have used flash X-ray imaging, witness plates, debris recovery, and numerical simulation to characterize the spatial, angular, and energy distributions of BAD (Huang et al., 2023; Ji et al., 2025; Wang et al., 2020; Wei et al., 2026; Xing et al., 2022).

These two research areas address different parts of the same penetration process. Existing models can determine the penetrator exit state and describe target perforation, material separation, and rear-surface bulging, but these quantities have not been systematically linked to the mass and geometric dispersion of target-plate-sourced debris. A direct engineering method that links penetrator and target parameters to the initial characteristics of target-derived debris has not yet been established.

This study develops an engineering model for calculating the mass and geometric dispersion of target-plate-sourced debris generated by long-rod penetration of finite-thickness steel plates. The model relates the penetrator exit state and rear-surface deformation and failure geometry to the target-plate-sourced debris mass, estimated central direction, and geometrically equivalent dispersion half-angles. Predictions are evaluated using rear-surface boundary data from eight shots, recovered debris masses from three shots, and perforation-center distributions on the first witness plates from three shots. The model provides an engineering link between long-rod penetration calculations and the initial characteristics of target-plate-sourced debris.

2. ENGINEERING MODEL FOR THE MASS AND GEOMETRIC DISPERSION OF TARGET-DERIVED DEBRIS

2.1. Equivalent partition and geometric representation of the rear surface

The initial mass and geometric dispersion of target-derived debris depend on the amount and spatial extent of target material removed or separated from the rear surface during penetration. During the late stage of penetration, direct material removal, outward deformation, fracture, and separation produce an irregular rear-surface morphology. For engineering calculation, the extents of these material states are represented by three nested characteristic boundaries.

As shown in Figure 1, the perforation boundary encloses the perforation region Ω_h and represents the extent of direct material removal. The material separation region Ω_{sep} lies between the perforation and material separation boundaries and represents the surrounding material affected by fracture and separation. Together, Ω_h and Ω_{sep} form the effective debris source region. The bulge region Ω_s lies between the material separation and bulge boundaries and consists of permanently deformed material remaining attached to the target plate. The total areas enclosed by the three boundaries are denoted by A_h, A_{sep}, and A_s, respectively. Accordingly, A_{sep} is the projected area of the effective debris source region, whereas the areas of the material separation and bulge regions are $A_{\mathrm{sep}} - A_h$ and $A_s - A_{\mathrm{sep}}$, respectively.

For subsequent calculations, the perforation boundary is represented by an area-equivalent circle with radius r_h, while the material separation and bulge boundaries are represented by ellipses with semiaxes a_{sep} and b_{sep}, and a_s and b_s, respectively. Under oblique penetration, their major axes are aligned with the incidence-plane direction and their minor axes with the transverse direction. Under normal penetration, the two semiaxes of each boundary are equal, and each ellipse reduces to a circle.

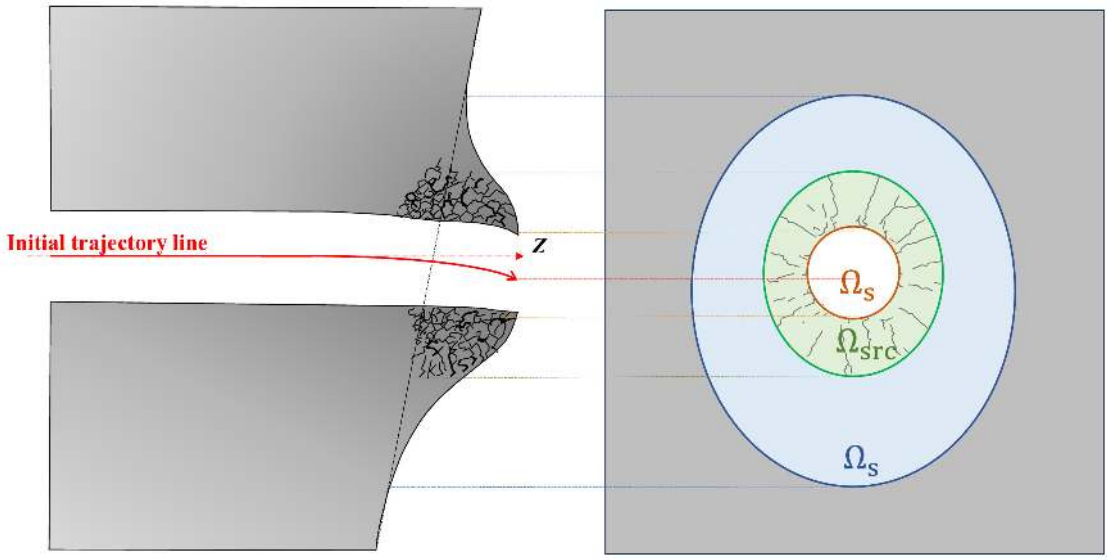


Figure 1 Schematic of the equivalent partition and characteristic boundaries of the rear surface.

2.2. Calculation of characteristic boundaries

Based on the equivalent rear-surface partition established in Section 2.1, the three characteristic boundaries are calculated sequentially. The perforation boundary provides the radial reference for the bulge boundary, and these two boundaries define the inner and outer references for the material separation boundary.

2.2.1. Perforation boundary

The equivalent perforation radius r_h is obtained from the empirical crater-radius relation in Ref. (2022):

$$r_h = \frac{d_p}{2}\left(1 + 0.0007 v_0\right). \tag{1}$$

where d_p is the maximum penetrator diameter and v_0 is the impact velocity in m/s. The enclosed area is $A_h = \pi r_h^2$.

2.2.2. Bulge boundary

The plastic influence zone ahead of the penetrator defines the bulge-development interval. Rear-surface bulging is described using the spherical-cap formulation of Ravid and Bodner (1983), and the maximum radius reached during this interval defines the bulge boundary.

The interaction region near the penetrator nose is represented by a hemisphere of radius $R_0 = d_p / 2$. The outer radius of the surrounding plastic zone is estimated using the cavity-expansion relation for a compressible elastic–plastic material (Xiaotong et al., 2026; Jiao and Chen, 2019). Let r_p denote this radius and $\alpha = r_p / R_0$ the corresponding radius coefficient. The coefficient α satisfies

$$\left(1+\frac{\rho_t u^2}{\sigma_{yt}}\right)\sqrt{K_t-\rho_t\alpha^2u^2}=\left(1+\frac{\rho_t\alpha^2u^2}{2G_t}\right)\sqrt{K_t-\rho_t u^2}. \tag{2}$$

where ρ_t is the target density, u is the cavity-expansion velocity, σ_{yt} is the dynamic yield strength, and K_t and G_t are the bulk and shear moduli, respectively. The determination of u and the material parameters is given in Ref. (2026).

The plastic-zone width beyond the penetrator nose is taken as the equivalent influence length:

$$\delta_p=r_p-R_0=(\alpha-1)R_0. \tag{3}$$

Because bulging develops near the end of penetration, the penetrator exit direction represents the equivalent penetration direction near the rear surface. Let β_0 be the initial angle between the penetrator direction and the target normal, and γ_f the exit deflection angle. The penetration angle at exit is

$$\psi_f=\beta_0+\gamma_f. \tag{4}$$

where ψ_f is the angle between the penetrator exit direction and the target normal. The sign of γ_f indicates deflection toward or away from the target normal. Approximating the near-exit trajectory as a straight path at ψ_f, the effective penetration path through a target of thickness t_t is

$$t_\psi=\frac{t_t}{\cos|\psi_f|}=t_t\sec|\psi_f|, \tag{5}$$

for normal penetration, $t_\psi=t_t$.

Taking the front-surface entry point as $z=0$, let z denote the penetrator-nose position along the equivalent penetration direction. As shown in **Figure 2**, bulging begins at $z=z_0$ when the plastic influence zone first reaches the rear surface and ends at $z=z_e$ when the penetrator nose reaches the rear surface. The initiation position is

$$z_0=t_\psi-\min\left(\delta_p,t_\psi\right). \tag{6}$$

If $\delta_p\geq t_\psi$, Equation (6) gives $z_0=0$. The termination position is $z_e=t_\psi$, and $z_0\leq z\leq z_e$ defines the bulge-development interval.

At position z, the remaining distance to the rear surface is $t_\psi-z$. Using this distance and r_h as the axial and radial references, the spherical-cap relations are

$$\eta_b=\frac{t_\psi-z}{r_h}\tan\beta_b+1, \tag{7}$$

$$\left[\frac{t_\psi-z}{r_h}\tan\beta_b+1\right]^3-\frac{3\sin^3\beta_b\left(z-z_0\right)}{r_h\left(1-\cos\beta_b\right)^2\left(2+\cos\beta_b\right)}=0. \tag{8}$$

where β_b is the spherical-cap geometry angle and η_b is the ratio of the bulge outer radius to the perforation radius. For each z, Equation (8) is solved for β_b, and Equation (7) then gives η_b. The instantaneous bulge radius is

$$R_b(z)=\eta_b(z)r_h. \tag{9}$$

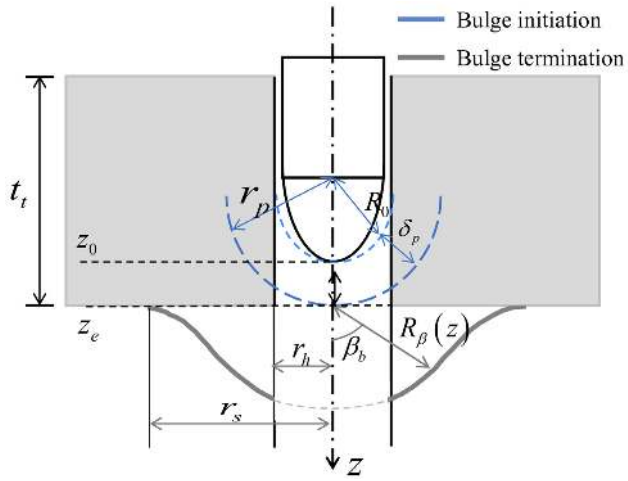


Figure 2 Schematic of the bulge initiation and termination positions and the spherical cap parameters.

The maximum radius over the bulge-development interval is

$$R_s = \max_{z_0<z<z_e} R_b(z). \tag{10}$$

Using $z_e = t_\psi$,

$$R_s = r_h \max_{z_0<z<t_\psi} \left[\frac{t_\psi - z}{r_h} \tan\beta_b(z) + 1 \right]. \tag{11}$$

Under oblique penetration, projecting an axisymmetric bulge normal to the equivalent penetration direction onto the rear-surface plane increases its incidence-plane dimension by $\sec|\psi_f|$. This value is taken as the limiting aspect ratio for fully developed directional elongation. Because bulging develops over only part of the effective penetration path, the degree of elongation is represented by the ratio of the bulge-development interval to that path:

$$\eta_\psi = \frac{t_\psi - z_0}{t_\psi} = \frac{\min\left(\delta_p, t_\psi\right)}{t_\psi}, \qquad 0 \le \eta_\psi \le 1. \tag{12}$$

The bulge-boundary aspect ratio is approximated by linear interpolation between the circular and limiting projected states:

$$\Gamma_s = 1 + \eta_\psi \left(\sec|\psi_f| - 1\right). \tag{13}$$

where $\Gamma_s = a_s / b_s$. Equation (13) gives $\Gamma_s = 1$ at $\eta_\psi = 0$ and $\Gamma_s = \sec|\psi_f|$ at $\eta_\psi = 1$. The major semiaxis and enclosed area are $a_s = \Gamma_s R_s$, $b_s = R_s$ and $A_s = \pi a_s b_s = \pi \Gamma_s R_s^2$, respectively. Under normal penetration, $\psi_f = 0$ gives $\Gamma_s = 1$ and $a_s = b_s = R_s$.

2.2.3. Material separation boundary

Local cracking and material separation generally produce an irregular material separation boundary (Sen et al., 2022; Teng and Wierzbicki, 2005; Virazels et al., 2025). Its overall geometry is estimated using the perforation and bulge boundaries as the inner and outer references. As an engineering approximation, its semiaxes are obtained by midpoint interpolation between the corresponding dimensions:

$$a_{\text{sep}} = \frac{r_h + a_s}{2}, \tag{14}$$

$$b_{\text{sep}} = \frac{r_h + b_s}{2}. \tag{15}$$

The enclosed area is

$$A_{\text{sep}} = \pi a_{\text{sep}} b_{\text{sep}} = \frac{\pi}{4}(r_h + a_s)(r_h + b_s). \tag{16}$$

The area expansion coefficient describes the relative position of the material separation boundary between the perforation and bulge boundaries:

$$\lambda_f = \frac{A_{\text{sep}} - A_h}{A_s - A_h}. \tag{17}$$

Substituting $A_h = \pi r_h^2$, Equation (16), and $A_s = \pi a_s b_s$ into Equation (17) gives

$$\lambda_f = \frac{a_s b_s + r_h(a_s + b_s) - 3r_h^2}{4\left(a_s b_s - r_h^2\right)}. \tag{18}$$

Under normal penetration, $a_s = b_s = R_s$, and the material separation boundary becomes a circle of radius $r_{\text{sep}} = \frac{r_h + R_s}{2}$. Thus, $A_{\text{sep}} = \pi r_{\text{sep}}^2$ and

$$\lambda_f = \frac{R_s + 3r_h}{4(R_s + r_h)}. \tag{19}$$

Because the material separation boundary is interpolated from the perforation and bulge boundaries, its predicted variation is governed by these two boundaries. The influence of this approximation on the model results is discussed in Section 4.

2.3. Calculation of target-derived debris mass

Target-derived debris mass is estimated from an equivalent source volume defined by the perforation and material separation boundaries and the effective participating thickness. The characteristic axial plug length in the Ravid and Bodner formulation represents the depth of material separated near the rear surface (1983). Projecting this length from the equivalent penetration direction onto the target thickness direction gives the effective participating thickness.

At a penetrator-nose position, the characteristic axial plug length is written as

$$l_p\left(z_p\right)=R_0\sqrt{\left[\frac{3\left(z_p-z_0\right)}{2R_0}\right]^{2/3}-1} \tag{20}$$

The plug length is evaluated when the penetrator nose reaches the rear surface, i.e.,

$$z_p=z_e=t_\psi \tag{21}$$

The corresponding characteristic plug length is therefore

$$l_{p,e}=R_0\sqrt{\left[\frac{3\left(t_\psi-z_0\right)}{2R_0}\right]^{2/3}-1} \tag{22}$$

Under oblique penetration, $l_{p,e}$ is measured along the equivalent penetration direction, and its projection onto the target-thickness direction is t_{eff}. Taking the physical target thickness as the upper bound gives

$$t_{\text{eff}}=\min\left\{R_0\cos\left|\psi_f\right|\sqrt{\left[\frac{3\left(t_\psi-z_0\right)}{2R_0}\right]^{2/3}-1},t_t\right\} \tag{23}$$

The first term in Equation (23) is the characteristic plug length projected onto the target-thickness direction, while the minimum operator prevents the calculated participating thickness from exceeding the physical target thickness. Equation (23) applies when

$$\frac{3\left(t_\psi-z_0\right)}{2R_0}>1 \tag{24}$$

This condition ensures that the term inside the square root is positive and that the characteristic plug length is real. It is the applicability condition of the adopted plug-length relation rather than an additional empirical criterion. If this condition is not satisfied, the characteristic participating depth cannot be determined using Equation (20), and the present debris-mass formulation is not applicable. All test conditions considered in this study satisfy this condition. The effective participating thickness ratio is defined as $C_t=t_{\text{eff}}/t_t$.

For the mass calculation, the perforation and material separation sections are represented by area-equivalent circular sections with areas A_h and A_{sep}, respectively. As shown by the blue shaded region in **Figure 3**, the effective debris source region extends from the perforation section at the inner end of the effective layer to the material separation section at the rear surface. Its depth is t_{eff}, and its equivalent radius is assumed to vary linearly through this thickness. The resulting equivalent source volume is a conical frustum with an equivalent mean cross-sectional area of

$$A_{\text{eq}}=\frac{A_h+A_{\text{sep}}+\sqrt{A_hA_{\text{sep}}}}{3}. \tag{25}$$

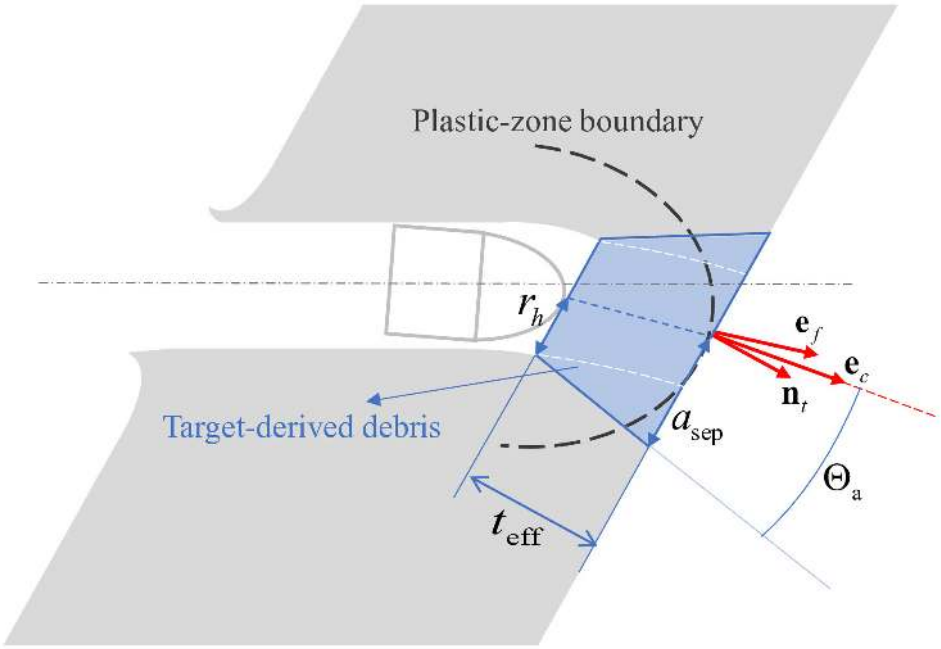


Figure 3. Incidence-plane schematic of the effective debris source region and geometrically equivalent dispersion of target-derived debris under oblique penetration.

The estimated target-derived debris mass is

$$m_t = \rho_t A_{\text{eq}} t_{\text{eff}}. \tag{26}$$

where ρ_t is the target material density and A_{eq} is the equivalent mean cross-sectional area of the effective debris source region.

2.4. Calculation of the central dispersion direction and geometrically equivalent dispersion half-angles of target-derived debris

Oblique penetration and exit-path deflection can bias the target-derived debris field (Goldsmith, 1999; Heider et al., 2004). The rear-surface normal represents the outward direction of target material release, while the penetrator exit direction reflects the influence of the near-exit penetration path. The two unit directions are assigned equal weight, and their internal angular bisector provides an engineering estimate of the central dispersion direction.

Let $\mathbf{n}_t$ denote the unit normal to the rear surface directed into the space behind the target plate, and let $\mathbf{e}_f$ denote the unit vector along the penetrator exit direction. The estimated central dispersion direction is

$$\mathbf{e}_c = \frac{\mathbf{n}_t + \mathbf{e}_f}{\left|\mathbf{n}_t + \mathbf{e}_f\right|}. \tag{27}$$

The central dispersion direction defines the field axis, while its angular extent is obtained from the expansion of the effective debris source region shown in **Figure 3**. Across t_{eff}, the area-equivalent section expands from the perforation boundary at the inner end of the effective layer to the material separation boundary at the rear surface. The corresponding slopes define the geometrically equivalent dispersion half-angles.

Under oblique penetration, the geometrically equivalent dispersion half-angles in the incidence-plane and transverse directions are

$$\Theta_a = \arctan\left(\frac{a_{\text{sep}} - r_h}{t_{\text{eff}}}\right), \tag{28}$$

$$\Theta_b = \arctan\left(\frac{b_{\text{sep}} - r_h}{t_{\text{eff}}}\right). \tag{29}$$

where Θ_a and Θ_b correspond to the incidence-plane and transverse directions, respectively. The effective participating thickness t_{eff} is calculated using Equation (23).

Under normal penetration, $\psi_f = 0$ and the material separation boundary becomes circular. The geometrically equivalent dispersion half-angle is

$$\Theta_s = \arctan\left(\frac{r_{\text{sep}} - r_h}{t_{\text{eff}}}\right). \tag{30}$$

In this case, $\Theta_a = \Theta_b = \Theta_s$. Because $\mathbf{e}_f = \mathbf{n}_t$, Equation (27) gives $\mathbf{e}_c = \mathbf{n}_t$. Together, $\mathbf{e}_c$ and the corresponding geometrically equivalent dispersion half-angle or half-angles define the axis and angular extent of the geometrically equivalent target-derived debris field.

3. ROD PENETRATION TESTS ON FINITE-THICKNESS STEEL TARGET PLATES AND DATA PROCESSING

3.1. Test arrangement and shot conditions

Eight rod penetration shots were conducted to validate the proposed model. As shown in Figure 4, the test projectile was launched from a $30\,\text{mm}$ ballistic gun located $15.5\,\text{m}$ from the target, with the muzzle center $1.3\,\text{m}$ above the ground. Two velocity screens were placed in front of the target; the nearer screen was approximately $1\,\text{m}$ from the target surface, and the screen spacing was $1.5\,\text{m}$. Their measurements were used to verify the impact velocity obtained from high-speed imaging in front of the target. A sabot arresting plate was placed between the muzzle and the velocity screens. The target plate was clamped to the target frame, and the support structure was adjusted to set the initial penetration angle. High-speed cameras in front of and behind the target recorded the impact and exit processes and provided the impact and residual velocities.

The witness pack recorded perforations produced by behind-armor debris and retained debris for recovery. It comprised 10 rubber plates alternating with 9 kraft paper sheets. The rubber plates measured $600\,\text{mm} \times 600\,\text{mm} \times 10\,\text{mm}$, and the paper sheets measured $600\,\text{mm} \times 530\,\text{mm} \times 2\,\text{mm}$. The paper sheets were centered on the rubber plates, and the pack was secured to its frame by four steel rods. The first rubber plate behind the target plate served as the first witness plate.

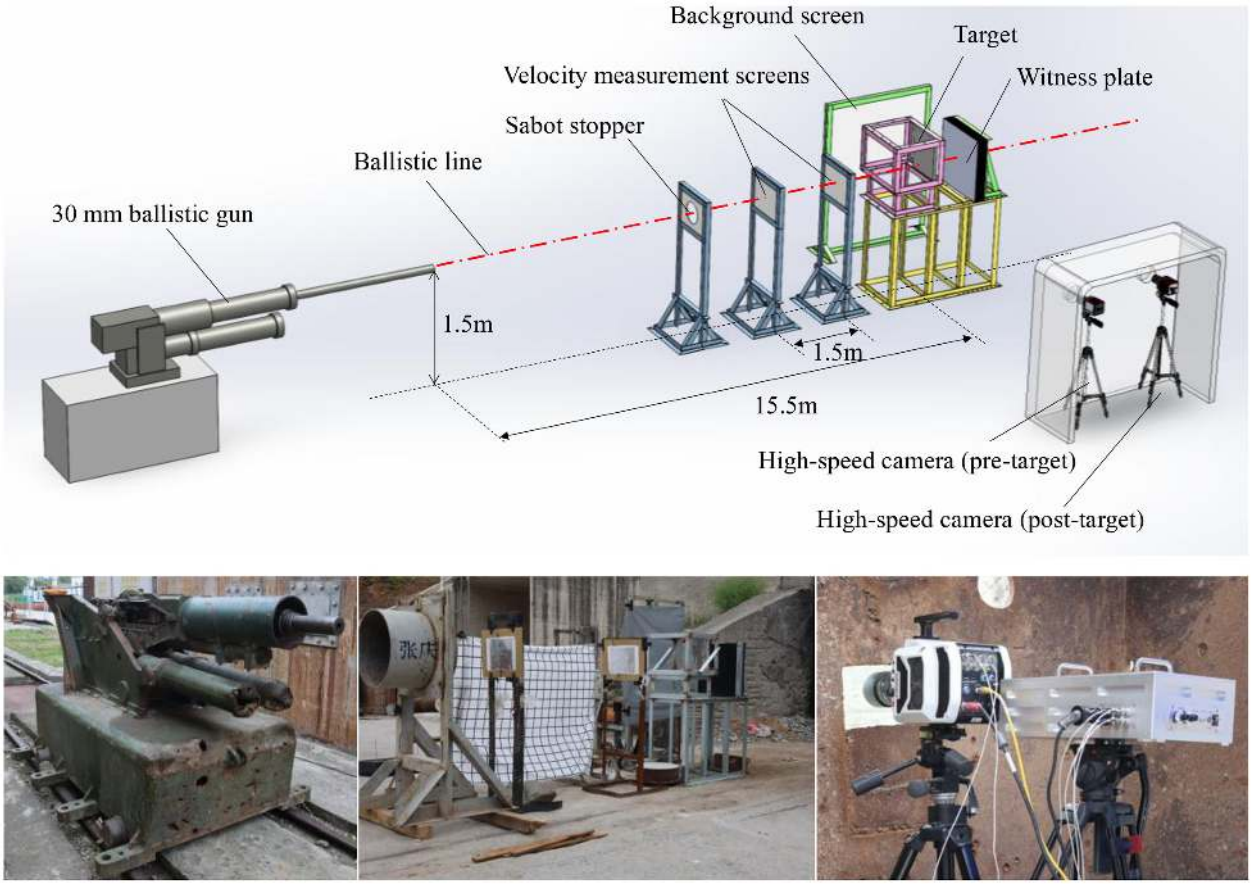


Figure 4 Test arrangement.

The 603 armor-steel target plates measured $400\,\text{mm}\times350\,\text{mm}\times30\,\text{mm}$, with a thickness of $t_t=30\,\text{mm}$ and a density of $\rho_t=7.80\times10^3\,\text{kg/m}^3$. The test projectile is shown in Figure 5. The projectile assembly had a total mass of approximately $260\,\text{g}$, including a sabot of approximately $72\,\text{g}$. The penetrator had a maximum diameter of $d_p=16\,\text{mm}$, a length of approximately $62\,\text{mm}$, and a density of $\rho_p=17.60\times10^3\,\text{kg/m}^3$. Its overall length with the fins and windshield installed was approximately $90\,\text{mm}$.



Figure 5 Test projectile.

Shots 1–4 were conducted without a witness pack or debris recovery device to maintain an unobstructed view for high-speed imaging. Because the camera triggering did not capture debris-field formation, only the rear-surface images were retained to extract the perforation, material separation, and bulge boundaries.

The witness pack and debris recovery device were installed for Shots 5–8. Shots 5 and 6 involved normal penetration, while Shots 7 and 8 had an initial penetration angle of 45°. Rear-surface images from all eight shots were used for boundary extraction, and the bulge-boundary aspect ratios from Shots 7 and 8 were used to evaluate the oblique-penetration direction correction. In Shot 8, the low impact point caused some debris to strike the target frame, affecting the debris trajectories and recovered mass. Shot 8 was therefore retained only for rear-surface boundary analysis. The target-derived debris masses and perforation-center distributions on the first witness plate from Shots 5–7 were used to evaluate the corresponding model predictions.

Table 1 lists the shot conditions and main measured parameters. Here, β_0 is the initial penetration angle, v_0 the impact velocity, v_{res} the residual velocity, and L_w the distance from the rear surface of the target plate to the first witness plate along the projectile trajectory. A dash indicates that no witness pack was installed.

Table 1 Shot conditions and main measured parameters.

Shot	1	2	3	4	5	6	7	8
β_0 / (°)	0	0	0	0	0	0	45	45
v_0 / (m/s)	974	963	993	962	916	746	941	943
v_{res} / (m/s)	840.02	823.94	858.56	822.96	767.20	540.97	678.03	679.90
L_w / cm	—	—	—	—	36.6	37.4	36.4	38.1

3.2. Post-test data processing

3.2.1. Extraction of rear-surface boundaries

The rear-surface images were scale-calibrated using the tape measure visible in each photograph. The perforation boundary, material separation boundary, and bulge boundary were then extracted sequentially. Contour segments obscured by shadows, adhered material, or local discontinuities were manually reviewed and corrected. The perforation boundary was identified as the outer edge of the material-loss region produced by complete perforation; cracked material remaining attached to the perforation edge was excluded. The material separation boundary was identified as the outer edge of the rear-surface traces associated with material fracture and separation. The bulge boundary was identified as the outer edge of the permanent plastic deformation traces on the rear surface. **Figure 6** shows the extracted boundaries for all eight shots.

The areas enclosed by the extracted contours are denoted by $A_{h,\mathrm{exp}}$, $A_{\mathrm{sep,exp}}$, and $A_{s,\mathrm{exp}}$, following the notation in Section 2. The area-equivalent radius of the perforation boundary is

$$r_{h,\mathrm{exp}} = \sqrt{\frac{A_{h,\mathrm{exp}}}{\pi}}. \tag{31}$$

The material separation and bulge boundaries were represented by equivalent ellipses. For each closed region, the enclosed area was calculated from the contour, and the aspect ratio was obtained from the equivalent ellipse defined by the second central moments of the region. An area-equivalent ellipse preserving the extracted area and aspect ratio was then constructed, with major and minor semiaxes $a_{i,\mathrm{exp}}$ and $b_{i,\mathrm{exp}}$, respectively. Under oblique penetration, the major axis of the equivalent bulge ellipse was aligned parallel to the incidence plane. The corresponding enclosed area and aspect ratio are

$$A_{i,\mathrm{exp}} = \pi a_{i,\mathrm{exp}} b_{i,\mathrm{exp}}, \qquad \Gamma_{i,\mathrm{exp}} = \frac{a_{i,\mathrm{exp}}}{b_{i,\mathrm{exp}}}, \qquad i \in \{\mathrm{sep}, s\}. \tag{32}$$

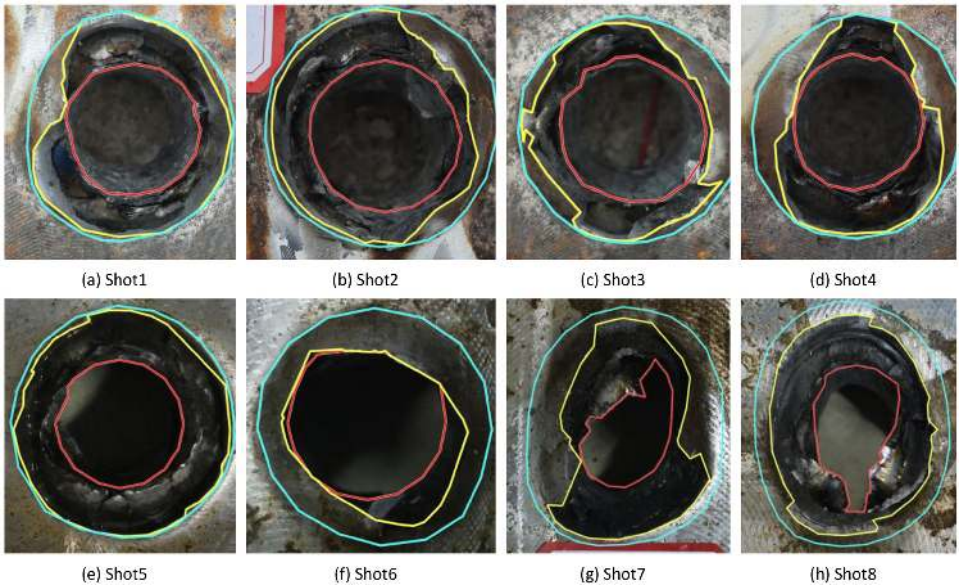


Figure 6 Extraction results for the three rear-surface boundaries in Shots 1–8.

The experimental area expansion coefficient was calculated using Equation (17). Table 2 summarizes the geometric parameters extracted from the rear-surface boundaries.

Table 2 Geometrical extraction results for the target plate back face boundaries.

Shot	$A_{h,\mathrm{exp}}$ / mm^2	$A_{\mathrm{sep,exp}}$ / mm^2	$\Gamma_{\mathrm{sep,exp}}$	$A_{s,\mathrm{exp}}$ / mm^2	$\Gamma_{s,\mathrm{exp}}$	$\lambda_{f,\mathrm{exp}}$
1	480.50	1215.50	1.20	2076.57	1.00	0.461
2	575.80	1104.00	1.13	2166.75	1.02	0.332
3	580.90	1083.40	1.23	2270.34	1.01	0.297
4	520.40	1008.20	1.39	1967.94	1.00	0.337
5	444.20	1313.30	1.04	1780.70	1.00	0.650
6	374.70	578.10	1.27	1573.70	1.00	0.170
7	488.80	1308.00	1.69	2099.70	1.21	0.509
8	569.40	1696.00	1.36	2325.20	1.25	0.642

3.2.2. Determination of the recovered target-derived debris mass

After each shot, the witness pack was disassembled layer by layer, and debris pieces embedded in the rubber plates were individually removed and classified by material origin. Magnetic response was used for preliminary classification. For pieces with adhered materials that could not be reliably classified in this manner, volume was measured by water displacement, and the calculated density was compared with those of the target plate and penetrator materials. Loose rubber and other surface attachments were manually removed before weighing. The debris pieces were weighed using an electronic balance with a capacity of $500\,\mathrm{g}$ and a resolution of $0.01\,\mathrm{g}$.

All recovered target-derived steel debris was weighed together, and its mass was denoted by $m_{t,\mathrm{rec}}$. Projectile-derived items, including the residual rod, penetrator erosion debris, sabot, fins, and windshield, were excluded. $m_{t,\mathrm{rec}}$ therefore represents only the recovered and identified target-derived debris and excludes unrecovered material. The valid recovered masses for Shots 5–7 were $69.28\,\mathrm{g}$, $74.31\,\mathrm{g}$, and $68.58\,\mathrm{g}$, respectively.

3.2.3. Extraction of perforation data from the first witness plate

Perforation data were extracted from images of the surface facing the target after each shot. Perspective correction was performed using the four corners of the first witness plate. A coordinate system was then established on the first witness plane, with the y-axis parallel to the incidence-plane direction and the x-axis aligned with the transverse direction. The measured relative position between the target plate and the first witness plate was used to register the perforation centers with the model projection.

After perspective correction, the center coordinates and area of each perforation were extracted. The residual-rod perforation, P_r, was identified from its position and shape and excluded from the behind-armor debris perforation data. Overlapping perforations with distinguishable contours were separated along concave boundary segments; regions that could not be separated reliably were treated as single compound perforations.

Figure 7 shows the perforation-center distributions for Shots 5–7. Marker size and color indicate perforation area. The measured perforation-center distributions were compared with the calculated geometrically equivalent dispersion ranges projected onto the first witness plane.

4. RESULTS AND DISCUSSION

The calculated rear-surface boundaries, target-derived debris mass, and geometrically equivalent dispersion range are compared with the corresponding experimental data. The analysis evaluates whether the model describes the overall rear-surface failure extent, estimates the target-derived debris mass from the two-dimensional boundaries and effective participating thickness, and captures the main spatial extent of the measured perforation distribution after projection onto the first witness plane. The limitations of the midpoint interpolation, effective participating thickness approximation, and oblique-penetration directional correction are also discussed.

4.1. Areas enclosed by the three rear-surface boundaries

The shot parameters in Table 1 and the calculated penetration angle at exit ψ_f were used to determine the areas enclosed by the perforation, material separation, and bulge boundaries. **Figure 8**(a) compares the model predictions with the experimentally extracted values.

For all eight shots, the calculated areas satisfy $A_{h,m} < A_{\mathrm{sep},m} < A_{s,m}$. The mean relative errors in the areas enclosed by the perforation, material separation, and bulge boundaries are 11.42%, 17.22%, and 9.13%, respectively. The perforation area is generally overestimated, with a mean signed relative error of 10.08%, indicating a consistent positive bias in the perforation-radius relation under the current shot conditions. The mean signed relative error in the bulge area

is −2.28%, showing no pronounced systematic overestimation or underestimation. The bulge-area error combines the effects of the calculated perforation radius, the plastic influence length obtained from the cavity-expansion model, and the bulge-development model.

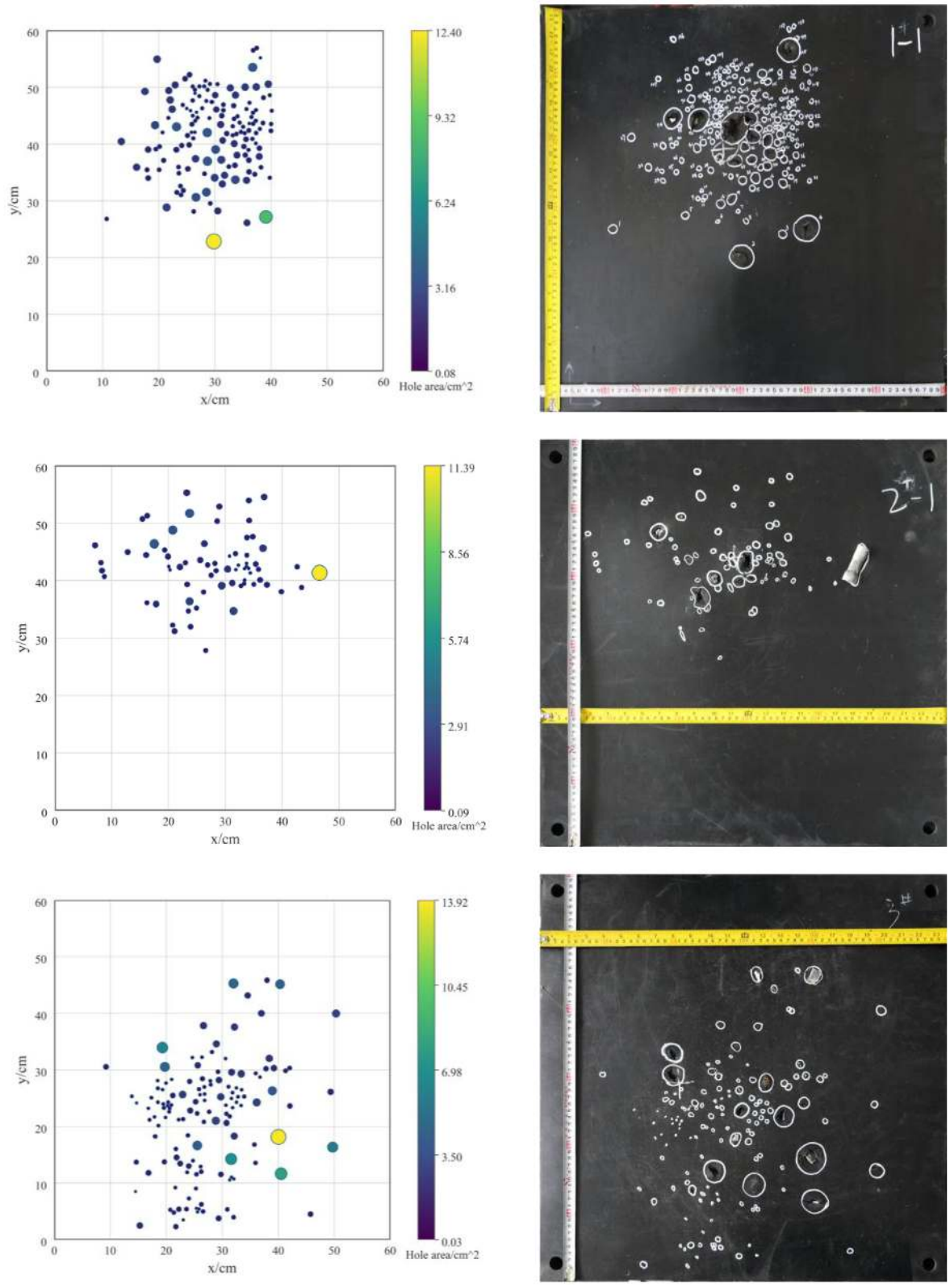


Figure 7 Distribution of debris perforations on the first witness plate

Under normal penetration, the calculated perforation area increases with impact velocity. The calculated bulge area reaches a relatively high value at approximately 916 m/s and then decreases slightly. Increasing impact velocity enlarges the perforation radius but reduces the calculated plastic influence length. The former increases the radial reference of the bulge region, whereas the latter limits bulge development. The calculated bulge area is therefore governed by their combined effect. Because the material separation boundary is obtained by midpoint interpolation between the perforation and bulge semiaxes, its variation is constrained by these two boundaries.

For Shots 7 and 8, the calculated perforation areas remain comparable to those for normal penetration at similar impact velocities, while the bulge boundaries elongate along the incidence-plane direction. The directional correction factors calculated from $\eta_\psi = \min(\delta_p, t_\psi)/t_\psi$ are 0.751 and 0.749, respectively. The corresponding calculated bulge-boundary aspect ratios are both 1.23, compared with the experimentally extracted values of 1.21 and 1.25. The mean relative errors in the bulge and material separation areas for these two shots are 5.47% and 12.60%, respectively. These results indicate that the directional correction can estimate the bulge-boundary aspect ratio under the current 45° oblique-penetration condition.

Figure 8(b) compares the experimentally derived area expansion coefficients $\lambda_{f,\mathrm{exp}}$ with the model predictions $\lambda_{f,m}$. The predicted values range from 0.416 to 0.429, whereas the experimental values range from 0.170 to 0.650. Midpoint interpolation constrains the material separation boundary to a narrow relative position between the perforation and bulge boundaries and therefore cannot reproduce its shot-to-shot variation. The largest errors in the material separation area occur in Shots 6 and 8, for which the model overestimates and underestimates the experimentally extracted areas, respectively. The relative errors for the other shots range from 1.31% to 14.98%.

The material separation boundary error includes the propagated errors from the perforation and bulge boundaries and the additional error introduced by midpoint interpolation. This uncertainty is subsequently transferred to the calculated target-derived debris mass and geometrically equivalent dispersion half-angles.

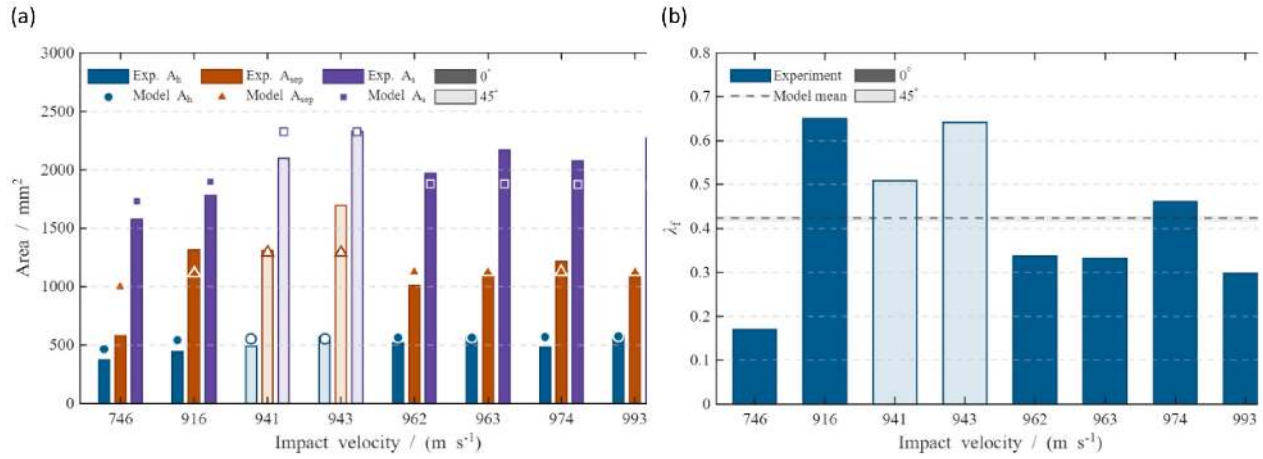


Figure 8 Comparison of the areas enclosed by the three rear-surface boundaries and the area expansion coefficient: (a) model predictions and experimentally extracted areas; (b) calculated and experimentally derived area expansion coefficients.

4.2. Target-derived debris mass

According to Equation (23), the effective participating thicknesses for Shots 5–7 are 11.77, 11.77, and 8.93 mm, respectively. For Shots 5 and 6, the plastic influence zone covers the full target thickness, so the finite-thickness constraint gives the same t_{eff}. Substituting $A_{h,m}$, $A_{\mathrm{sep},m}$, and t_{eff} into Equations (25) and (26) gives the target-derived debris mass. As shown in **Figure 9**, the relative errors are 7.55%, 11.69%, and 9.00%, with a mean relative error of 9.41%.

The calculated mass depends on the equivalent mean cross-sectional area and effective participating thickness. For Shots 5 and 7, the larger material separation area and smaller effective participating thickness of Shot 7 partly offset in the equivalent source volume. Shots 5 and 6 have the same effective participating thickness, so their mass difference is mainly governed by the boundary areas.

The main uncertainties arise from the calculated boundaries, effective participating thickness, and conical-frustum approximation. Boundary errors and midpoint interpolation affect the equivalent mean cross-sectional area, while the latter two approximations simplify the irregular source geometry and participating depth. Incomplete recovery of small debris pieces and classification uncertainty may also affect the recovered mass.

The mean relative error of 9.41% indicates good agreement between the calculated and recovered masses and supports the applicability of the formulation under the tested conditions.

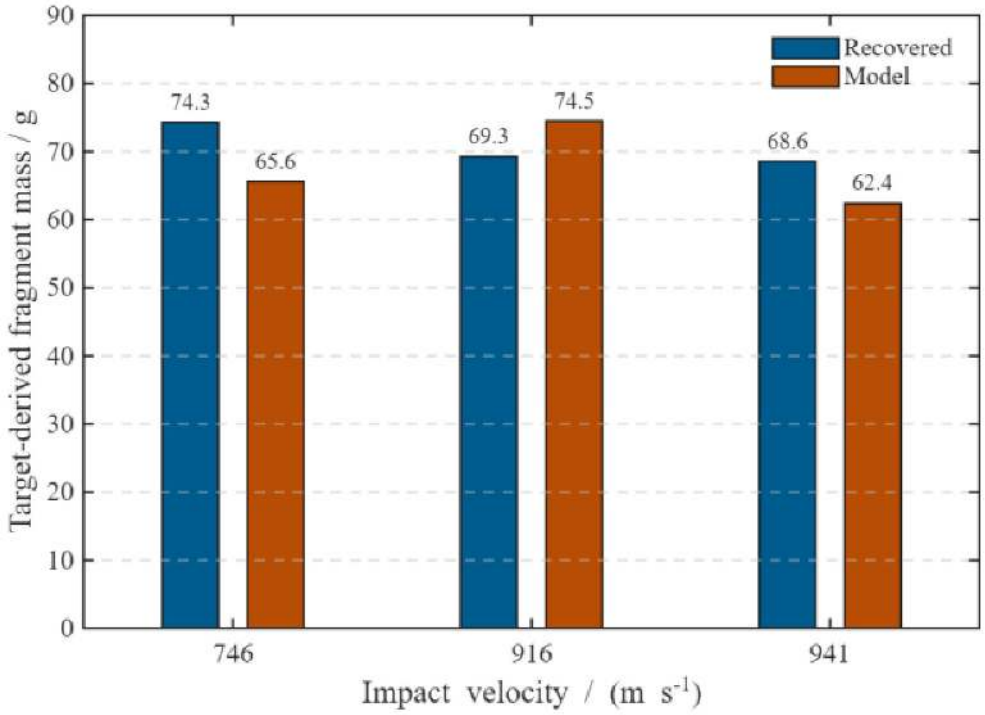


Figure 9 Comparison of the calculated and recovered target-derived debris masses.

4.3. Projection of the geometrically equivalent dispersion range

The calculated central dispersion direction and corresponding geometrically equivalent dispersion half-angle or half-angles define the dispersion range. This range was projected onto the first witness plane using the measured test geometry. After excluding the residual-rod perforation, it was compared with the measured perforation-center distribution using the coverage ratio and angular extent.

The central dispersion direction determines the projection center C_b. The projection is circular under normal penetration and elliptical under oblique penetration, with its major axis parallel to the incidence plane. The perforation-center coverage ratio is $P_{\text{in}} = N_{\text{in}} / N_{\text{all}} \times 100\%$, where N_{in} and N_{all} are the numbers of measured perforation centers inside the model projection and in the complete distribution, respectively. The signed angular difference is $\Delta\Theta = \Theta_m - \Theta_{\text{exp}}$,and the relative error is $|\Delta\Theta| / \Theta_{\text{exp}} \times 100\%$, where Θ_m and Θ_{exp} are the model half-angle and measured angular extent, respectively. The comparison results are summarized in **Table 3**.

Table 3 Comparison of the model projections with the measured perforation-center distributions on the first witness plates.

Shot	Comparison direction	N_{in} / N_{all}	P_{in} / %	Model half-angle/(°)	Measured angular extent/(°)	Angular difference/(°)	Relative error/%
5	Radial	136/140	97.14	25.94	26.49	−0.55	2.07
6	Radial	67/69	97.10	25.62	25.84	−0.22	0.83*
7	Incidence-plane direction	132/133	99.25	43.47	33.60	+9.87	29.37
7	Transverse direction	132/133	99.25	32.28	32.28	0.00	0.01*

*Relative errors were calculated using unrounded values.

As shown in **Figure 10**(a) and (b), the model projections contain 136 of 140 perforation centers for Shot 5 and 67 of 69 for Shot 6, giving coverage ratios of 97.14% and 97.10%, respectively. The relative errors in the radial angular extent are 2.07% and 0.83%. The projections therefore cover nearly all measured perforation centers and reproduce the radial extent under normal penetration.

For Shot 7, the model projection contains 132 of 133 perforation centers, giving a coverage ratio of 99.25%, as shown in **Figure 10**(c). The calculated transverse half-angle is 32.28°, consistent with the measured angular extent. The calculated incidence-plane half-angle is 43.47°, compared with a measured angular extent of 33.60°, giving a relative error of 29.37%. The incidence-plane elongation introduced by the bulge-boundary directional correction and midpoint interpolation is transferred too strongly to the projected range. The model reproduces the transverse extent but overpredicts the incidence-plane extent. The geometrically equivalent half-angles in Equation (28)–(29) use the expansion slopes of the effective debris source region as an approximation to the angular spread of the debris velocity field. The incidence-plane overprediction indicates that the initial debris velocity field is less anisotropic than the static source geometry. The debris velocity distribution generated during material separation may therefore weaken the incidence-plane directionality inherited from the rear-surface boundaries. Because the present tests do not resolve the initial velocity components of the target-derived debris, this effect cannot be quantified independently.

The projected ranges contain more than 97% of the measured perforation centers for all three shots. The main deviation is the overprediction of the incidence-plane extent for Shot 7.

4.4. Model performance and limitations

Overall, the model provides reasonable engineering estimates of the principal rear-surface boundaries, target-derived debris mass, and the main extent of the perforation-center distribution. The perforation and bulge boundary areas are reproduced with comparatively consistent accuracy, while the material separation boundary captures the average separation scale but shows less shot-to-shot variation than the experiments. Combined with the effective participating thickness, the calculated boundaries give target-derived debris masses close to the recovered values. The predicted dispersion ranges also describe the radial extent under normal penetration and the transverse extent under oblique penetration.

The main discrepancies are associated with the simplified treatment of the material separation boundary and the directional dispersion under oblique penetration. The fixed midpoint interpolation restricts the material separation boundary to a narrow relative position between the perforation and bulge boundaries and therefore smooths its variation among different shots. Because this boundary is subsequently used to determine the equivalent debris source area and dispersion half-angles, the associated uncertainty also affects the predicted debris mass and dispersion range.

Under oblique penetration, the expansion slopes of the effective debris source region are used as an approximation to the angular spread of the debris velocity field. The overprediction of the incidence-plane extent for Shot 7 indicates that the initial debris velocity field is less anisotropic than the static rear-surface geometry. The velocity distribution generated during material separation may therefore weaken the incidence-plane directionality inherited from the rear-surface boundaries, but this effect cannot be quantified independently from the present first-witness-plane data. The angular-bisector assumption for the central dispersion direction also remains to be independently evaluated, and the recovered-mass comparison is subject to debris recovery and material-classification uncertainties.

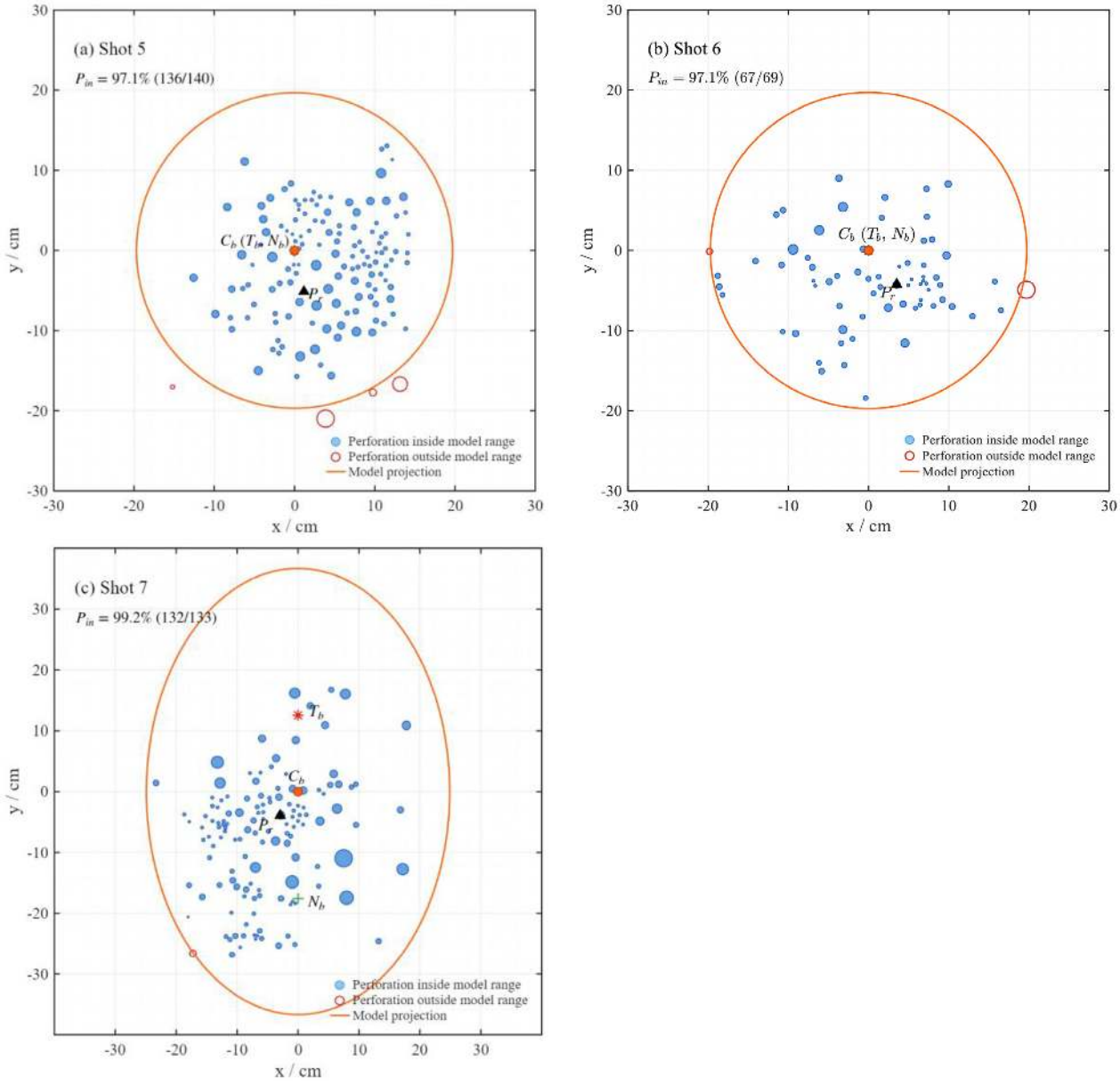


Figure 10. Comparison of projected geometrically equivalent dispersion ranges and measured perforation-center distributions on the first witness plates: (a) Shot 5; (b) Shot 6; (c) Shot 7.

The present validation includes both normal and oblique penetration and covers the principal model outputs through rear-surface boundary measurements, recovered target-derived debris masses, and first-witness-plane perforation distributions. Because the formulation is expressed in terms of penetrator dimensions and residual state,

target thickness and material parameters, and rear-surface boundary geometry, its applicability is not restricted to the specific penetrator and target configuration used in the experiments. The current results support its use as an engineering method for rod penetration of finite-thickness steel targets when the assumed perforation, bulging, and material-separation mechanisms remain applicable. For substantially different penetrator geometries, target materials, relative target thicknesses, or penetration regimes, the model may remain applicable in principle, although its predictive accuracy requires further independent evaluation, particularly for the directional dispersion under oblique penetration.

5. CONCLUSIONS

This study developed an engineering method for calculating the mass and geometric dispersion of target-derived debris generated by rod penetration of finite-thickness steel plates. The method links the penetrator exit state and rear-surface deformation and failure geometry to the target-derived debris mass, central dispersion direction, and geometrically equivalent dispersion half-angles. The main conclusions are as follows.

(1) The three-boundary representation provides a consistent geometric description of material removal, separation, and permanent deformation on the rear surface. The model reproduces the nested relationship among the perforation, material separation, and bulge boundaries and captures the incidence-plane elongation of the bulge boundary under oblique penetration. Midpoint interpolation provides an overall estimate of the material separation boundary but smooths its shot-to-shot variation.

(2) Combining the equivalent mean cross-sectional area with the effective participating thickness provides a practical estimate of target-derived debris mass. The calculated and recovered masses have a mean relative error of 9.41%, showing that the dominant debris source volume can be represented using two-dimensional rear-surface boundaries and an effective participating depth.

(3) The projected geometrically equivalent dispersion ranges contain more than 97% of the measured perforation centers. The model reproduces the radial extent under normal penetration and the transverse extent under oblique penetration. Its main deviation is the excessive incidence-plane extent, indicating that the directional elongation of the static bulge boundary is transferred too strongly to the calculated debris dispersion range.

Author's Contribution: Xiaotong Qi: Conceptualization, methodology, formal analysis, investigation, data curation, validation, visualization, and writing – original draft. Yangziyi Ji: Investigation, validation, and writing – review and editing. Xiangdong Li: Conceptualization, resources, supervision, project administration, funding acquisition, and writing – review and editing. Lanwei Zhou: Resources, supervision, funding acquisition, and writing – review and editing.

Data Availability: All relevant data supporting the findings of this study are available from the corresponding authors upon reasonable request.

Editor: Marcilio Alves.

References

Arnold, W. and Paul, W. (2001). Behind armor debris investigation and their application into a new vulnerability model. International Journal of Impact Engineering 26: 21–32.

Backman, M. E. and Goldsmith, W. (1978). The mechanics of penetration of projectiles into targets. International Journal of Engineering Science 16: 1–99.

Børvik, T., Langseth, M., Hopperstad, O. S. and Malo, K. A. (1999). Ballistic penetration of steel plates. International Journal of Impact Engineering 22: 855–886.

Chocron, S., Anderson, C. E., Jr., Walker, J. D. and Ravid, M. (2003). A unified model for long-rod penetration in multiple metallic plates. International Journal of Impact Engineering 28: 391–411.

Dey, S., Børvik, T., Hopperstad, O. S., Leinum, J. R. and Langseth, M. (2004). The effect of target strength on the perforation of steel plates using three different projectile nose shapes. International Journal of Impact Engineering 30: 1005–1038.

Đurović, R., Elek, P., Marković, M. and Jevtić, D. (2025). Modification and experimental validation of the Forrestal-Warren perforation model for high hardness armor steel plates of intermediate thickness. Defence Technology 46: 267–284.

Forrestal, M. J. and Luk, V. K. (1988). Dynamic spherical cavity expansion in a compressible elastic-plastic solid. Journal of Applied Mechanics 55: 275–279.

Goldsmith, W. (1999). Non-ideal projectile impact on targets. International Journal of Impact Engineering 22: 95–395.

Hartmann, M. (2005). Behind-armour debris—modelling and simulation. A litterature review. Report No. FOI-R--1678--SE, Swedish Defence Research Agency, Tumba.

Heider, N., Weber, K. and Weidemaier, P. (2004). Experimental and numerical simulation analysis of the impact process of structured KE penetrators onto semi-infinite and oblique plate targets. In: Proceedings of the 21st International Symposium on Ballistics, Adelaide, Australia, 19–23 April 2004, pp. 97–103.

Huang, X., Li, W., Li, W., Yin, G., Wang, Y. and Guo, T. (2023). Energy spatial distribution of behind-armor debris generated by penetration of explosively formed projectiles with different length–diameter ratio. Applied Sciences 13: 2665.

Ji, Y., Li, X., Hu, B., Zhou, L. and Liu, X. (2025). Vulnerability analysis of satellite under the impact hypervelocity projectile considering the formation of behind-plate debris. International Journal of Aeronautical and Space Sciences 26: 629–649.

Jiao, W. and Chen, X. (2019). Review on long-rod penetration at hypervelocity. Advances in Mechanics 49: 201904. (in Chinese)

Li, X., Zhou, L. and Ji, Y. (2022). Target Vulnerability Assessment and Its Applications. Beijing Institute of Technology Press, Beijing. (in Chinese)

Ma, Y., Tang, K., Hou, Y., Gong, H., Gu, M., Wang, J., Li, Y., Ma, T. and Wang, J. (2025). Experimental and numerical investigation on the oblique penetration of jacketed long-rod projectiles into spaced targets. International Journal of Impact Engineering 206: 105463.

Mayseless, M., Sela, N., Stilp, A. J. and Hohler, V. (1992). Behind the armor debris distribution function. In: Proceedings of the 13th International Symposium on Ballistics, Vol. 2, Stockholm, Sweden, 1–3 June 1992, pp. 77–85.

Qi, X., Ji, Y., Fu, J., Li, X. and Zhou, L. (2026). A ballistic trajectory deflection model for long-rod oblique penetration of finite-thickness armor plates. Acta Mechanica Sinica 42: 460292.

Ravid, M. and Bodner, S. R. (1983). Dynamic perforation of viscoplastic plates by rigid projectiles. International Journal of Engineering Science 21: 577–591.

Recht, R. F. and Ipson, T. W. (1963). Ballistic perforation dynamics. Journal of Applied Mechanics 30: 384–390.

Sen, S., Shaw, A. and Nayak, S. (2022). A mathematical model for perforation of metal plates through adiabatic shear plugging. International Journal of Impact Engineering 163: 104175.

Teng, X. and Wierzbicki, T. (2005). Dynamic shear plugging of beams and plates with an advancing crack. International Journal of Impact Engineering 31: 667–698.

Virazels, T., García-Molleja, J., Nieto-Fuentes, J. C., Gonzales, M., Sket, F. and Rodríguez-Martínez, J. A. (2025). High-velocity fragmentation and spall fracture of steel AF9628. International Journal of Plasticity 194: 104454.

Wang, X., Jiang, J., Sun, S., Men, J. and Wang, S. (2020). Investigation on the spatial distribution characteristics of behind-armor debris formed by the perforation of EFP through steel target. Defence Technology 16: 119–135.

Wei, G., Xu, H., Guo, R., Li, X., Zhang, L. and Ji, L. (2026). Spatial dispersion characteristics of behind-armor debris generated during the penetration of tantalum alloy explosively-formed projectile. Explosion and Shock Waves 46: 051433. (in Chinese)

Xing, B., Zhao, J., Chen, L., Hu, A., Zhu, F., Liu, J., Guo, R. and Hou, Y. (2022). Disperse characteristic of behind-armor debris formed by explosively formed penetrator vertically penetrating steel target. Transactions of Beijing Institute of Technology 42: 1026–1033. (in Chinese)

Yarin, A. L., Roisman, I. V., Weber, K. and Hohler, V. (2000). Model for ballistic fragmentation and behind-armor debris. International Journal of Impact Engineering 24: 171–201.

Yossifon, G. and Yarin, A. L. (2002). Behind-the-armor debris analysis. International Journal of Impact Engineering 27: 807–835.